We are IntechOpen, the world's leading publisher of Open Access books Built by scientists, for scientists

4,800
Open access books available

122,000
International authors and editors

135M
Downloads

Our authors are among the

154
Countries delivered to

TOP 1%
most cited scientists

12.2%
Contributors from top 500 universities

WEB OF SCIENCE™

Selection of our books indexed in the Book Citation Index in Web of Science™ Core Collection (BKCI)

Interested in publishing with us?
Contact book.department@intechopen.com

Numbers displayed above are based on latest data collected.
For more information visit www.intechopen.com

Chapter 2

A Quantum Trajectory Interpretation of Magnetic Resistance in Quantum Dots

Ciann-Dong Yang and Shih-Ming Huang

Additional information is available at the end of the chapter

http://dx.doi.org/10.5772/intechopen.74409

Abstract

For a complete description of the electronic motion in a quantum dot, we need a method that can describe not only the trajectory behavior of the electron but also its probabilistic wave behavior. Quantum Hamilton mechanics, which possesses the desired ability of manifesting the wave-particle duality of electrons moving in a quantum dot, is introduced in this chapter to recover the quantum-mechanical meanings of the classical terms such as backscattering and commensurability and to give a quantum-mechanical interpretation of the observed oscillation in the magneto-resistance curve. Solutions of quantum Hamilton equations reveal the existence of electronic standing waves in a quantum dot, whose occurrence is found to be accompanied by a jump in the electronic resistance. The comparison with the experimental data shows that the predicted locations of the resistance jump match closely with the peaks of the measured magneto-resistance.

Keywords: quantum dots, quantum Hamilton mechanics, standing waves, quantum trajectory, magneto-resistance

1. Introduction

As the size of electronic devices is narrowed down to the nanoscale, quantum effects become so prominent that classical mechanics is no longer able to provide an accurate description for electrons moving in nanostructures. However, due to the lack of the sense of trajectory in quantum mechanics, classical or semi-classical mechanics so far has been the sole tool in determining ballistic orbits in quantum dots. Classical orbits satisfying commensurability conditions of geometrical resonances were derived in the literature to determine the magneto-transport behavior of periodic quantum systems. It was reported that the observed regular peaks in the magneto-resistance corresponded to backscattering of commensurate orbits [1],

and the critical magnetic fields determined from the backscattering orbits showed an excellent agreement with the observed peak positions in the magneto-resistance curves [2]. A recent study showed that the ballistic motion of electrons within quantum dots can be controlled by an externally applied magnetic field so that the resulting conductance images resemble the classical transmitted and backscattered trajectories [3].

The use of an anisotropic harmonic function, instead of an abrupt hard potential, to describe the confining potential in a quantum dot was shown to be helpful to improve the accuracy of predicting magneto-resistance peaks based on backscattering orbits [4]. Nowadays, the confinement potential forming an electron billiard can be practically patterned to almost arbitrary profile, through which ballistic orbits with chaotic dynamics can be generated to characterize magneto transport [5]. However, the chaotic behavior and its change with magnetic field could not be described in the usual quantum-mechanical picture due to the lack of a trajectory interpretation. Regarding this aspect, the classical description becomes a valued tool for detailed understanding of the transition from low to high magnetic fields in quantum dot arrays [6]. On the other hand, quantum mechanical model for electron billiards was known as quantum billiards [7], in which moving point particles are replaced by waves. Quantum billiards are most convenient for illustrating the phenomenon of Fano interference [8] and its interplay with Aharonov-Bohm interference [9], which otherwise cannot be described by classical methods.

From the existing researches, we have an observation that the ballistic motion in electron billiards was solely described by classical mechanics, while the wave motion in quantum billiards could only be described by quantum mechanics. The aim of this chapter is to give a unified treatment of electron billiards and quantum billiards. We point out that quantum Hamilton mechanics [10, 11] can describe both ballistic motion and wave motion of electrons in a quantum dot to provide us with a quantum commensurability condition to determine backscattering orbits as well as with the wave behavior to characterize the magneto-resistance in a quantum dot.

Quantum Hamilton mechanics is a dynamical realization of quantum mechanics in the complex space [12], under which each quantum operator is realized as a complex function and each wavefunction is represented by a set of complex-valued Hamilton equations of motion. With quantum Hamilton mechanics, we can recover the quantum-mechanical meanings of the classical commensurability condition by showing that there are integral numbers of oscillation in the radial direction, as an electron undergoes a complete angular oscillation around a quantum dot. When the radial and angular dynamics are commensurable, the shape of electronic quantum orbits is found to be stationary like a standing wave. Furthermore, the wave number N, distributed on the circumference of the quantum dot, can be controlled by the applied magnetic field. It will be shown that the classical backscattering orbits discovered in the literature resemble the shape of the quantum standing waves derived here with their wave numbers equal to the numbers of electron's bounces within the quantum dot.

The electronic standing-wave motions considered in this chapter will reveal that a jump of the magneto-resistance in quantum dots is accompanied by a phenomenon of magnetic stagnation, which is a quantum effect that an electron is stagnated or trapped within a quantum dot

by an applied magnetic field in such a way that the electron's cyclotron angular velocity is exactly counterbalanced by its quantum angular velocity. We point out that magnetic stagnation is a degenerate case from the electronic standing-wave motion as the wave number N approaches to infinity. The magnetic fields yielding the phenomenon of magnetic stagnation can be determined by the quantum Hamilton equations derived here. Knowing these critical magnetic fields allows us to control the magneto-resistance precisely.

In the following sections, we first introduce quantum Hamilton mechanics and apply it to derive Hamilton equations, which are then used in Section 2 to describe the electronic quantum motions in a quantum dot. By solving the Hamilton equations of motion, Section 3 demonstrates electronic standing-wave motions in various quantum states and characterizes the magnetic field leading to the phenomenon of magnetic stagnation. In Section 4, we show that the magnetic stagnation is the main cause to the resistance oscillation of quantum dots in low magnetic field by comparing the theoretical predictions obtained from Section 3 with the experimental results of the magneto-resistance curve [4, 13].

2. Quantum Hamilton dynamics in a 2D quantum dot

To probe the quantum to classical transition, which involves both classical and quantum features, quantum dots are the most natural systems [14]. Analyzing such systems, we need an approach that can provide both classical and quantum descriptions. Quantum Hamilton mechanics is one of the candidates satisfying this requirement. This chapter will apply quantum Hamilton mechanics to an open quantum dot with circular shape, which is connected to reservoirs with strong coupling. The electronic transport through an open quantum dot can be realized by nano-fabrication techniques as a two-dimensional electron gases system (2DES) at an AlGaAs/GaAs heterostructure, as depicted in **Figure 1**.

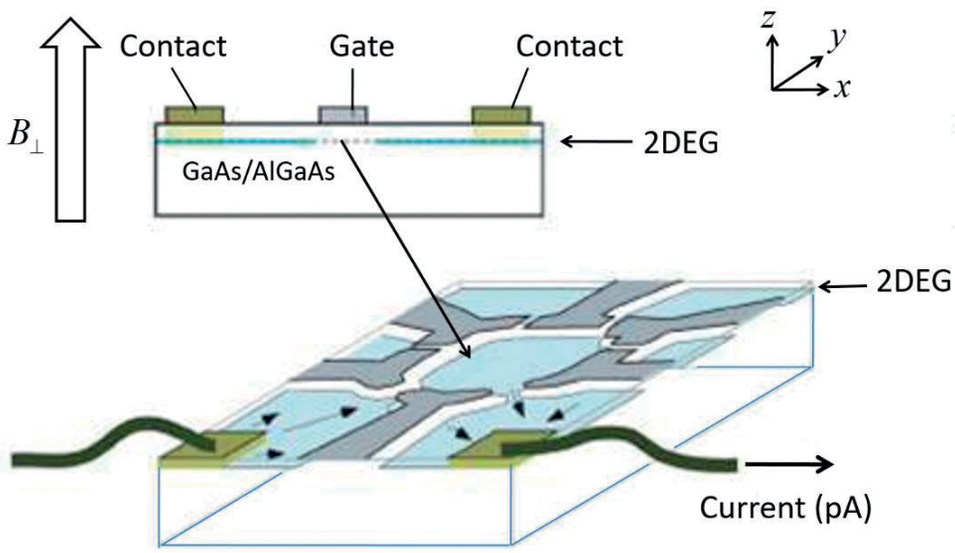

Figure 1. Schematic illustration of a semiconductor heterostructure with a circular dot between the two tunnel barriers.

Under the framework of quantum Hamilton mechanics [10, 12], the equivalent mathematical model of a quantum dot is described as an electron moving in an electromagnetic field with scalar potential V and vector potential $\mathbf{A}$. The related Hamiltonian operator $\widehat{H}$ can be realized as the following complex Hamiltonian function,

$$H(t,\mathbf{q},\mathbf{p}) = \frac{1}{2m}\left(\mathbf{p}+\frac{c}{e}\mathbf{A}\right)\cdot\left(\mathbf{p}+\frac{c}{e}\mathbf{A}\right) + V(t,\mathbf{q}) + \frac{\hbar}{2im}\nabla\cdot\mathbf{p}. \tag{1}$$

We adopt polar coordinates $\mathbf{q} = (r,\theta)$ and momentum $\mathbf{p} = (p_r, p_\theta)$ in the above equation to describe the electronic quantum motion in a 2D circular quantum dot. The resulting complex Hamiltonian Eq. (1) becomes

$$H = \frac{1}{2m^*}\left[\left(p_r+\frac{e}{c}A_r\right)^2 + \frac{1}{r^2}\left(p_\theta+\frac{e}{c}A_\theta\right)^2\right] + V(r,\theta) + \frac{\hbar}{2im^*}\left(\frac{1}{r}p_r + \frac{\partial p_r}{\partial r} + \frac{1}{r^2}\frac{\partial p_\theta}{\partial\theta}\right), \tag{2}$$

where $m^* = 0.067m_e$ is the electron's effective mass in AlGaAs/GaAs heterostructure. The scalar potential $V(r,\theta)$ acts as a confinement potential in the dot, and is modeled by the parabolic function $V = kr^2/2 = m^*\omega_0^2 r^2/2$ to simulate a soft-wall potential. The vector potential $\mathbf{A}$ is determined from the applied magnetic field $\mathbf{B}$ via the relation $\mathbf{B} = \nabla\times\mathbf{A}$. Here, we consider a constant $\mathbf{B}$ along the z direction, which amounts to $A_r = 0$ and $A_\theta = Br^2/2$. Substituting the above assignments of V and $\mathbf{A}$ into the complex Hamiltonian Eq. (2), we obtain

$$H = \frac{1}{2m^*}\left(p_r^2 + \frac{1}{r^2}p_\theta^2\right) + \omega_L p_\theta + \frac{1}{2}m^*\omega^2 r^2 + \frac{\hbar}{2im^*}\left(\frac{1}{r}p_r + \frac{\partial p_r}{\partial r} + \frac{1}{r^2}\frac{\partial p_\theta}{\partial\theta}\right) \tag{3}$$

where $\omega_L = eB/(2m^*c)$ is the Larmor frequency and $\omega = \sqrt{\omega_0^2+\omega_L^2}$ is the composite frequency. The quantum Hamilton-Jacobi equation associated with the Hamiltonian H defined in Eq. (1) reads

$$\frac{\partial S}{\partial t} + H(t,\mathbf{q},\mathbf{p})\Big|_{p_i=\partial S/\partial q_i} = 0, \tag{4}$$

where S is the quantum action function to be determined. By making use of the substitution

$$p_r = \frac{\partial S}{\partial r},\quad p_\theta = \frac{\partial S}{\partial\theta}, \tag{5}$$

the quantum Hamilton-Jacobi Eq. (4) associated with the Hamiltonian in Eq. (3) turns out to be

$$\frac{\partial S}{\partial t} + \frac{1}{2m^*}\left[\left(\frac{\partial S}{\partial r}\right)^2 + \frac{1}{r^2}\left(\frac{\partial S}{\partial\theta}\right)^2\right] + \omega_L\frac{\partial S}{\partial\theta} + \frac{1}{2}m^*\omega^2 r^2 - \frac{i\hbar}{2m^*}\left(\frac{1}{r}\frac{\partial S}{\partial r} + \frac{\partial^2 S}{\partial r^2} + \frac{1}{r^2}\frac{\partial^2 S}{\partial\theta^2}\right) = 0. \tag{6}$$

The recognition of the complex Hamiltonian H in Eqs. (1) and (3) as a complex realization of the Hamiltonian operator $\widehat{H}$ is confirmed by the fact that the quantum Hamilton-Jacobi equation in Eqs. (4) and (6) yields the same Schrodinger equation as constructed from $\widehat{H}$. This can be seen by applying the following transformation

http://dx.doi.org/10.5772/intechopen.74409

$$S = -i\hbar \ln \Psi, \tag{7}$$

to Eq. (6) to produce the expected Schrodinger equation:

$$i\hbar \frac{\partial \Psi}{\partial t} = -\frac{\hbar^2}{2m^*}\left(\frac{\partial^2 \Psi}{\partial r^2} + \frac{1}{r}\frac{\partial \Psi}{\partial r} + \frac{1}{r^2}\frac{\partial^2 \Psi}{\partial \theta^2}\right) - i\hbar\omega_L \frac{\partial \Psi}{\partial \theta} + \frac{1}{2}m^*\omega^2 r^2 \Psi. \tag{8}$$

Due to the time-independent nature of the applied potentials $\mathbf{A}$ and V, the wavefunction Ψ in Eq. (8) assumes the following form of solution,

$$\Psi(t, r, \theta) = e^{-iEt/\hbar}\psi(r, \theta), \tag{9}$$

where $\psi(r, \theta)$ satisfies the time-independent Schrodinger equation

$$\widehat{H}\psi \triangleq \left[-\frac{\hbar^2}{2m^*}\left(\frac{\partial^2}{\partial r^2} + \frac{1}{r}\frac{\partial}{\partial r} + \frac{1}{r^2}\frac{\partial^2}{\partial \theta^2}\right) - i\hbar\omega_L \frac{\partial}{\partial \theta} + \frac{1}{2}m^*\omega^2 r^2\right]\psi = E\psi. \tag{10}$$

On the other hand, Eq. (3) can be rewritten by using the substitutions Eqs. (5) and (7) as

$$\widehat{H}\psi = H\psi, \tag{11}$$

where H and $\widehat{H}$ are defined, respectively, by Eqs. (3) and (10). This is a direct proof of the fact that the complex Hamiltonian H is a functional realization of the Hamiltonian operator $\widehat{H}$ in a complex space. Indeed, it can be shown [10] that every quantum operator $\widehat{A}$ can be realized as a complex function A via the relation $\widehat{A}\psi = A\psi$. The combination of Eqs. (10) and (11) reveals the energy conservation law $H = E$, which is a natural result of Hamilton mechanics by noting that the Hamiltonian H in Eq. (3) does not contain time t explicitly and must be a motion constant equal to the system's total energy E.

Upon performing the differentiations $\partial p_r/\partial r$ and $\partial p_\theta/\partial \theta$ involved in Eq. (3), we have to specify in advance the action function S or equivalently the wavefunction ψ via the relation Eq. (7). This requirement makes the complex Hamiltonian H state-dependent. For a given quantum state described by ψ, the complex Hamiltonian H can be expressed explicitly as:

$$H = \frac{1}{2m^*}\left(p_r^2 + \frac{1}{r^2}p_\theta^2\right) + \omega_L p_\theta + \frac{1}{2}m^*\omega^2 r^2 + \frac{\hbar}{2im^*}\left(\frac{1}{r}p_r + \frac{\hbar}{i}\frac{\partial^2 \ln \psi}{\partial r^2} + \frac{1}{r^2}\frac{\hbar}{i}\frac{\partial^2 \ln \psi}{\partial \theta^2}\right). \tag{12}$$

Apart from deriving the Schrodinger equation, the above complex Hamiltonian also gives electronic quantum motions in the state ψ in terms of the Hamilton equations of motion,

$$\frac{dr}{dt} = \frac{\partial H}{\partial p_r} = \frac{1}{m^*}p_r + \frac{\hbar}{2im^*}\frac{1}{r} = \frac{\hbar}{im^*}\frac{\partial \ln \psi}{\partial r} + \frac{\hbar}{2im^*}\frac{1}{r}, \tag{13}$$

$$\frac{d\theta}{dt} = \frac{\partial H}{\partial p_\theta} = \frac{1}{m^* r^2}p_\theta + \omega_L = \frac{\hbar}{im^* r^2}\frac{\partial \ln \psi}{\partial \theta} + \omega_L. \tag{14}$$

The appearance of the imaginary number $i = \sqrt{-1}$ on the right-hand side of the above equations indicates that the quantum trajectory $(r(t), \theta(t))$ has to be defined in the complex space as $(r(t), \theta(t)) = (r_R(t) + ir_I(t), \theta_R(t) + i\theta_I(t))$ to guarantee the solvability of Eqs. (13) and (14). It is just the coupling connection between the real and imaginary parts that gives rise to the quantum phenomena, as we have observed in the real world, such as wave-particle duality [15], tunneling [16], and Heisenberg uncertainty principle [17]. For a given 1D wavefunction $\Psi(t, x)$ expressed in Cartesian coordinates, the complex Hamiltonian Eq. (1) has a simple form:

$$H(t, x, p) = \frac{1}{2m}p^2 + V(t, x) + \frac{\hbar}{2im}\frac{\partial p}{\partial x} = \frac{1}{2m}p^2 + V(t, x) - \frac{\hbar^2}{2m}\frac{\partial^2 \ln \Psi(t, x)}{\partial x^2}. \tag{15}$$

The Hamilton equation for x turns out to be

$$\dot{x} = \frac{\partial H}{\partial p} = \frac{p}{m} = \frac{1}{m}\frac{\partial S}{\partial x} = \frac{\hbar}{im}\frac{\partial \Psi}{\partial x}, \quad x \in \mathbb{C} \tag{16}$$

which can be conceived of as a complex-valued version of Bohmian mechanics [18, 19]. The complex quantum trajectory method based on Eq. (16) has been recently developed into a potential computational tool to analyze wave-packet interference [20] and wave-packet scattering [21].

The wavefunction ψ has to be solved in advance from the Schrodinger Eq. (10), before we determine the electron's quantum trajectory $(r(t), \theta(t))$ from Eqs. (13) and (14). In terms of the dimensionless radial distance $\rho = (\hbar/m\omega)^{-1/2}r$, the eigenvalues $E_{n,l}$ and the related eigenfunction $\psi_{n,l}$ can be solved analytically as [22].

$$E_{n,l} = (2n + |l| + 1)\hbar\omega + l\hbar\omega_L, \tag{17}$$

$$\psi_{n,l}(\rho, \theta) = R_{n,l}(\rho)\Theta_l(\theta) = C_{n,l}e^{-\rho^2/2}\rho^{|l|}L_n^{|l|}(\rho^2)e^{il\theta}, \tag{18}$$

where $n = 0, 1, 2, \cdots$ is the radial quantum number, $l = 0, \pm 1, \pm 2, \cdots$ is the angular quantum number, and $C_{n,l}$ is a normalization factor. The electronic motion in the eigenstate $\psi_{n,l}$ now can be established by integrating Eqs. (13) and (14) with ψ given by Eq. (18):

$$\frac{d\rho}{d\tau} = \frac{1}{i}\left(\frac{d \ln R_{n,l}(\rho)}{d\rho} + \frac{1}{2\rho}\right) \triangleq f_{n,l}(\rho), \tag{19}$$

$$\frac{d\theta}{d\tau} = \frac{l}{\rho^2} + \frac{\omega_L}{\omega}. \tag{20}$$

where the dimensionless time is expressed by $\tau = t\omega$. Eq. (20) indicates that the angular dynamics $\theta(\tau)$ is influenced by the magnetic field B via the relation $\omega_L = eB/(2m^*c)$ and reveals the existence of a critical B such that the Larmor angular velocity ω_L/ω counterbalances the quantum angular velocity l/ρ^2 to yield $d\theta/d\tau = 0$. The stagnation magnetic field denotes the critical B that stagnates the electron with zero angular displacement within a quantum dot. The occurrence of magnetic stagnation retards the electronic transport and causes a jump in

resistance. In the following sections, we will characterize the stagnation magnetic field from the equations of motion Eqs. (19) and (20) and verify the consistency between this theoretical prediction and the experimental measurement of resistance.

3. Standing waves and critical magnetic field

The conductivity of a quantum dot depends on how electrons move under the confinement potential within the quantum dot. Eqs. (19) and (20) provides us with all the required information to describe the underlying electronic quantum motion. The radial motion $\rho(\tau)$ described by Eq. (19) and the angular motion $\theta(\tau)$ described by Eq. (20) are, individually, periodic time functions, whose periods, T_ρ and T_θ, can be computed by using the residue theorem. In case that the radial and angular motions are not commensurable, i.e., $T_\rho/T_\theta \notin \mathbb{Q}$, the overall motion is not periodic and the electron's orbit precesses continuously around the periphery of the quantum dot, as shown in **Figure 2a**. By way of this precession orbit, an electron can pass through the quantum dot from the entrance to the exit and contribute to the conductance.

On the other hand, if T_ρ/T_θ is a rational number, the shape of the electron's orbit is stationary like a standing wave, as shown in **Figure 2b**. Except that the orientation of the standing wave happens to align with the direction from the entrance to the exit, as shown in **Figure 2c**, passage through the quantum dot is prohibited, when a standing-wave motion emerges. A standing-wave (non-precessing) orbit has to satisfy the commensurability condition,

$$T_\theta = NT_\rho \tag{21}$$

where N is a positive integer. This condition ensures that when the electron undergoes a complete oscillation in the θ direction, there are integral numbers of oscillation in the r direction. Once electronic standing waves emerge in a quantum dot, the electron after a complete θ revolution will return to the entrance to the quantum dot and consequently contribute to the resistance of the quantum dot.

As shown in **Figure 2d**, the standing-wave motion degenerates into a confined motion such that the electron is trapped into a closed trajectory, in the extreme case $N \to \infty$. When the electron is trapped or stagnated, it is in no way to pass through the quantum dot and causes a remarkable increase in resistance. The special magnetic field corresponding to $N \to \infty$ plays the major role in the magneto-resistance and is to be derived below.

The pattern and the orientation of the standing waves can be controlled by the applied magnetic field B via the relation Eq. (20), which indicates that the angular motion depends on the parameter,

$$\frac{\omega_L}{\omega} = \frac{\omega_L}{\sqrt{\omega_0^2 + \omega_L^2}} = \frac{eB/(2m^*c)}{\sqrt{\omega_0^2 + e^2B^2/(2m^*c)^2}}, \tag{22}$$

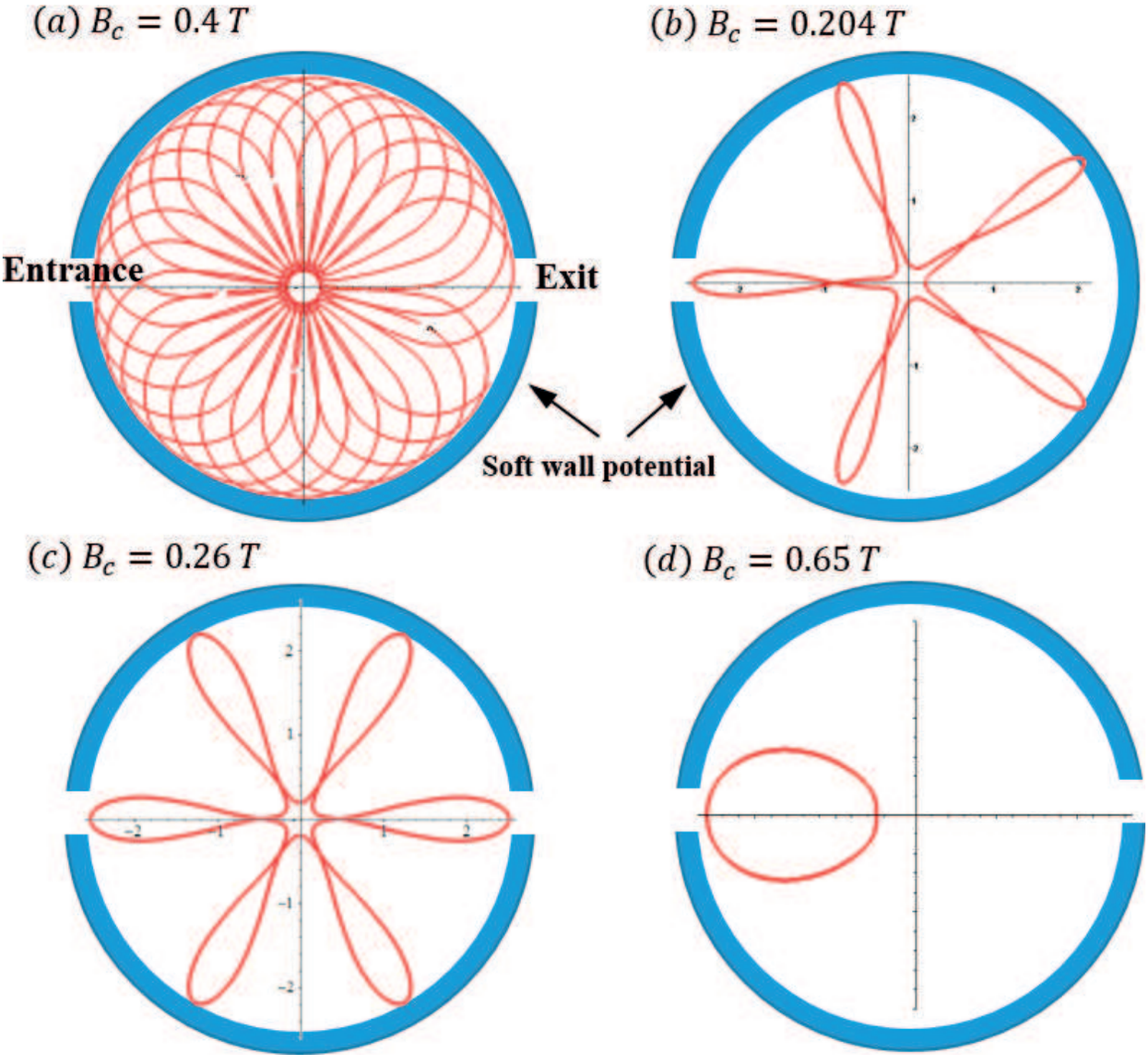

Figure 2. Four types of electronic quantum trajectory in a quantum dot. (a) a magnetic field ($B_c = 0.4T$) not satisfying the commensurability condition Eq. (21) yields precessing trajectories. (b) A critical magnetic field $B_c = 0.204T$ yields standing-wave like quantum trajectory, whose five wavelengths on the circumference do not contact the exit of the quantum dot. (c) A magnetic field $B_c = 0.26T$ yields similar standing-wave trajectory as that in part (b) but with six wavelengths which contact both the entrance and exit of the quantum. (d) At $B_c = 0.65T$, a stagnation magnetic field, the electron is stagnated within an isolated region of θ.

which, in turn, is solely determined by the magnetic field B. We are able to control the resistance of the quantum dot by varying the magnitude of B to satisfy the commensurability condition Eq. (21). Our next issue is to characterize the critical magnetic field B_c that satisfies the commensurability condition Eq. (21). The period T_ρ in Eq. (21) can be evaluated by the radial dynamics Eq. (19). The radial motion $\rho(t)$ is a periodic time function whose trace on the complex ρ plane forms a closed path c_ρ, along which the period T_ρ can be computed as a contour integral as

$$T_\rho = \int d\tau = \oint_{c_\rho} \frac{d\rho}{f_{n,l}(\rho)}. \tag{23}$$

According to the residue theorem, the contour integral in Eq. (23) is equal to $2\pi i$ times the sum of the residues of $1/f_{n,l}(\rho)$ evaluated at its poles within the contour c_ρ, i.e.,

$$T_\rho = \oint_{c_\rho} \frac{d\rho}{f_{n,l}(\rho)} = 2\pi i \sum_k R_k, \tag{24}$$

where R_k is the residue of $1/f_{n,l}(\rho)$ evaluated at its k^{th} pole. Let Ω_k be the set containing all of contours which enclose the same poles of $1/f_{n,l}(\rho)$. According to the residue theorem, the integrals along the contours belonging to the same set Ω_k have the same contour integral, denoted by $T_\rho^{(k)}$. If the number of different ways of pole encirclement is M, we can define M contour sets, Ω_1, Ω_2, …, Ω_M, with each contour set corresponding to one particular way of pole encirclement. Along all the possible contours, the period T_ρ defined by Eq. (23) can only have M discrete values, $T_\rho^{(1)}$, $T_\rho^{(2)}$, …, $T_\rho^{(M)}$, defined by

$$T_\rho = \oint_{c_\rho} \frac{d\rho}{f_{n,l}(\rho)} = T_\rho^{(k)}, \quad \forall c_\rho \in \Omega_k, \quad k = 1, 2, \cdots, M. \tag{25}$$

The sequence $\left\{T_\rho^{(1)}, T_\rho^{(2)}, \cdots, T_\rho^{(M)}\right\}$ then constitutes a set of quantization levels for the period T_ρ in the quantum state $\psi_{n,l}(\rho, \theta)$.

(A) Standing Wave with *l*=0

In case of $l = 0$, the radial dynamics and azimuth dynamics are decoupled according to Eqs. (19) and (20). A look on the ground state $(n, l) = (0, 0)$ is helpful to understand some common features in the states with $l = 0$. The related wavefunction is given by Eq. (18) as $R_{0,0}(\rho) = e^{-\rho^2/2}$ and $\Theta_0(\theta) = 1$. Substituting this wavefunction into Eqs. (19) and (20) yields the equations of motion for the ground-state electron,

$$\frac{d\rho}{d\tau} = i\frac{2\rho^2 - 1}{2\rho}, \quad \frac{d\theta}{d\tau} = \frac{\omega_L}{\omega}. \tag{26}$$

It appears that that the ground-state electron rotates with a constant angular velocity ω_L/ω around its equilibrium radial position $\rho_{eq} = \sqrt{2}/2$. Therefore, the azimuth period T_θ is simply $2\pi/(\omega_L/\omega)$, and the radial period T_ρ can be computed from Eqs. (24) and (26) as

$$T_\rho = \frac{1}{i}\oint_{c_\rho} \frac{2\rho}{2\rho^2 - 1} d\rho = \pi, \tag{27}$$

where c_ρ is any contour enclosing the pole $\rho_{eq} = \sqrt{2}/2$ on the complex plane of ρ.

The commensurability condition Eq. (21) with the calculated T_ρ and T_θ for the ground state turns out to be

$$\frac{\omega_L}{\omega} = \frac{2}{N}, \quad N = 3, 4, 5, \cdots, \tag{28}$$

where we note $\omega_L/\omega < 1$ from its definition in Eq. (22). The critical magnetic field B_c now can be solved from Eq. (28) as

$$B_c = \frac{B_0}{\sqrt{N^2/4 - 1}}, \quad N = 3, 4, 5, \cdots, \tag{29}$$

where B_0 is the magnetic field whose Larmor frequency ω_L is equal to the natural frequency ω_0 of the harmonic oscillator, i.e., $B_0 = (2m^*c/e)\omega_0$. The relation expressed by Eq. (29) characterizes all the magnetic fields that force the electron to behave like a standing wave in the ground state of a quantum dot.

Regarding excited states, there are multiple periods in the radial motion $\rho(\tau)$ as indicated by Eq. (25). Taking first excited state $(n, l) = (1, 0)$ as an illustrating example, the quantum dynamics is described by

$$\frac{d\rho}{d\tau} = i\frac{2\rho^4 - 11\rho^2 + 6}{2\rho(\rho^2 - 2)} \quad \frac{d\theta}{d\tau} = \frac{\omega_L}{\omega}, \tag{30}$$

which has four equilibrium points at

$$\rho_{eq} = \pm\frac{\sqrt{11 \pm \sqrt{73}}}{2} \tag{31}$$

According to different encirclements of equilibrium points, four sets of complex trajectories $\rho(\tau)$ can be identified as shown in **Figure 3a**, where Ω_1 and Ω_2 denote the sets of all trajectories enclosing only one equilibrium point, Ω_3 denotes the set enclosing two equilibrium points, and Ω_4 denotes the set enclosing all the four equilibrium points.

Corresponding to the four different ways of encirclement, the four quantization levels of T_ρ can be computed from Eq. (24) as

$$T_\rho = \frac{2\pi\left(73 \pm 3\sqrt{73}\right)}{292}, \pi, 2\pi. \tag{32}$$

The commensurability condition for the occurrence of standing wave in the four contour sets now can be derived from Eq. (21) as

$$\frac{\omega_L}{\omega} = \left\{ \begin{array}{lll} \frac{73 + 3\sqrt{73}}{16N}, N \geq 7, & \rho(\tau) \in \Omega_1 \\ \frac{73 - 3\sqrt{73}}{16N}, N \geq 3, & \rho(\tau) \in \Omega_2 \\ \frac{2}{N}, \quad N \geq 3, & \rho(\tau) \in \Omega_3 \\ \frac{1}{N}, \quad N \geq 2, & \rho(\tau) \in \Omega_4 \end{array} \right\} \tag{33}$$

http://dx.doi.org/10.5772/intechopen.74409

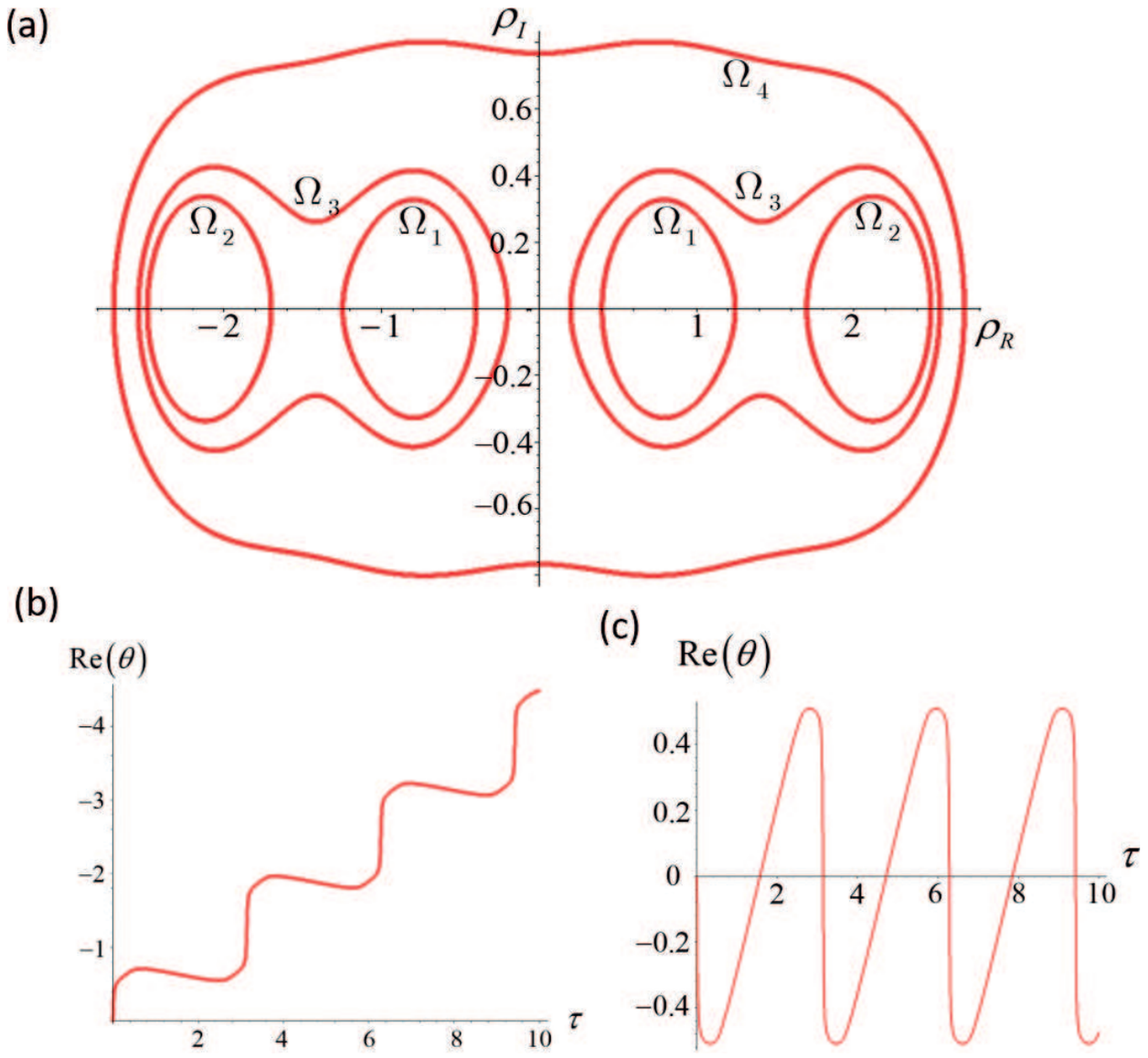

Figure 3. (a) Four sets of complex trajectories $\rho(\tau)$ are identified according to different encirclements of equilibrium points in the state $(n,l)=(1,0)$. (b) Typical time response of an increasing $\mathrm{Re}(\theta)$ corresponds to the trajectory shown in Figure 2b. (c) Typical time response of an oscillatory $\mathrm{Re}(\theta)$ corresponds to the trajectory shown in Figure 2d.

The related critical magnetic field B_c can be determined by substituting Eq. (33) into Eq. (22). Comparing Eq. (28) with Eq. (33), we can see that the critical B_c, which raises standing waves in the ground state, also raises standing waves in the first excited state. The peaks of the magneto-resistance just concentrate on the dominant critical magnetic field that concurrently produces standing waves in different states.

(B) Standing Wave with $l > 0$.

In the case of $l > 0$, the cyclotron angular velocity ω_L/ω and the quantum angular velocity l/ρ^2 are in the same direction so as to give an intensified resultant $\dot{\theta} = l/\rho^2 + \omega_L/\omega$. The coupling between the azimuth motion $\theta(\tau)$ and the radial dynamics $\rho(\tau)$ makes the evaluation of T_θ more difficult; however, because $\rho(\tau)$ is a periodic function, we can evaluate $\dot{\theta}$ in Eq. (20) by simply replacing l/ρ^2 with its average value $\left(l/\rho^2\right)_{ave}$, if only the period of $\theta(\tau)$ is concerned,

$$T_\theta = \frac{2\pi}{\dot{\theta}_{ave}} = \frac{2\pi}{(l/\rho^2)_{ave} + \omega_L/\omega} = NT_\rho. \tag{34}$$

The time average $(l/\rho^2)_{ave}$ is computed over one period of $\rho(\tau)$ and can be converted into a contour integral along the contour c_ρ traced by $\rho(\tau)$ on the complex plane:

$$\left(\frac{l}{\rho^2}\right)_{ave} = \frac{l}{T_\rho}\int_0^{T_\rho} \frac{d\tau}{\rho^2(\tau)} = \frac{l}{T_\rho}\oint_{c_\rho} \frac{d\rho}{\rho^2 f_{n,l}(\rho)}. \tag{35}$$

Substituting the above $(l/\rho^2)_{ave}$ into Eq. (34), we obtain the critical value of ω_L/ω as

$$\frac{\omega_L}{\omega} = \frac{2\pi}{NT_\rho} - \left(\frac{l}{\rho^2}\right)_{ave}. \tag{36}$$

Due to the constraint $0 \le \omega_L/\omega \le 1$, the admissible integer N lies in the interval

$$\frac{2\pi/T_\rho}{1 + (l/\rho^2)_{ave}} < N \le \frac{2\pi/T_\rho}{(l/\rho^2)_{ave}}, \tag{37}$$

where T_ρ and $(l/\rho^2)_{ave}$ are given by Eqs. (24) and (35), respectively. The admissible range of N is narrowed by increasing angular quantum number l, as can be seen from inequality Eq. (37). There is a maximum allowable l beyond which inequality Eq. (37) has no integer solution and standing-wave motion within the quantum dot disappears. To compare with the quantum state $(n,l) = (1,0)$ considered previously, let us study the state $(n,l) = (1,1)$ whose quantum motion is described by

$$\frac{d\rho}{d\tau} = i\frac{2\rho^4 - 11\rho^2 + 6}{2\rho(\rho^2 - 2)}, \quad \frac{d\theta}{d\tau} = \frac{1}{\rho^2} + \frac{\omega_L}{\omega}. \tag{38}$$

The period T_ρ is the same as that derived in Eq. (32), and the period T_θ can be computed by Eq. (34) with $(l/\rho^2)_{ave}$ evaluated by the contour integral Eq. (35) as

$$\left(\frac{1}{\rho^2}\right)_{ave} = \begin{Bmatrix} l\left(11 + \sqrt{73}\right)/12, & \rho(\tau) \in \Omega_1 \\ l\left(11 - \sqrt{73}\right)/12, & \rho(\tau) \in \Omega_2 \\ 2l/3, & \rho(\tau) \in \Omega_3 \cup \Omega_4 \end{Bmatrix} \tag{39}$$

Using T_ρ and $(l/\rho^2)_{ave}$ in Eqs. (36) and (37), the critical value of ω_L/ω in the state $(n,l) = (1,1)$ becomes

$$\frac{\omega_L}{\omega}\begin{Bmatrix} \dfrac{73 + 3\sqrt{73}}{16N} - \dfrac{11 + \sqrt{73}}{12}, N = 3, & \rho(\tau) \in \Omega_1 \\ \dfrac{73 - 3\sqrt{73}}{16N} - \dfrac{11 - \sqrt{73}}{12}, 3 \le N \le 14, & \rho(\tau) \in \Omega_2 \\ 2/N - 2/3, N = 2, 3, & \rho(\tau) \in \Omega_3 \\ 1/N - 2/3, N = 1, & \rho(\tau) \in \Omega_4 \end{Bmatrix} \tag{40}$$

The comparison between Eqs. (33) and (40) leads to the observation that the number of the allowed integer N decreases dramatically when l increases from 0 to 1. Since the total different number of N accounts for the number of different ways by which standing wave can be formed, the possibility for the occurrence of standing-wave motion and thus the electronic resistance decreases with increasing angular quantum number l. The main reason is that the increment of the angular velocity $\dot{\theta} = l/\rho^2 + \omega_L/\omega$ with large l accelerates the electron's angular motion around the quantum dot and thus improves the conductance of the quantum dot.

(C) Standing Waves with $l < 0$

In this case, the cyclotron angular velocity ω_L/ω and the quantum angular velocity l/ρ^2 are in opposite directions so as to give a weakened resultant $\dot{\theta} = l/\rho^2 + \omega_L/\omega$. The resultant angular velocity $\dot{\theta}_{ave}$ may be positive, negative or zero, depending on the magnitude of $\left(l/\rho^2\right)_{ave}$, which can be classified into three categories: (1) $\left(l/\rho^2\right)_{ave} \geq 0$, (2) $-1 < \left(l/\rho^2\right)_{ave} < 0$, and (3) $\left(l/\rho^2\right)_{ave} \leq -1$, as listed in **Table 1**.

The cases of $l = 0$ and $l > 0$ considered previously belong to category (1) with $\dot{\theta}_{ave} > 0$, while the case of $l < 0$ belongs to categories (2) and (3). Taking into account the motion with $\dot{\theta}_{ave} < 0$, Eq. (36) now becomes

$$\frac{\omega_L}{\omega} = \pm\frac{2\pi}{NT_\rho} - \left(\frac{l}{\rho^2}\right)_{ave}, \tag{41}$$

where the admissible integer N for the three categories is summarized in **Table 1**.

The critical magnetic field B_c given by Eq. (41) with $\dot{\theta}_{ave} > 0$ and $\dot{\theta}_{ave} < 0$ produces standing-wave motions oscillating, respectively, counterclockwise and clockwise around the quantum dot, as shown in **Figure 2b** and **c**. For an angular quantum number with $-1 < \left(l/\rho^2\right)_{ave} < 0$ in category (2), there exists a special Larmor angular velocity ω_L/ω such that it counterbalances the quantum angular velocity $\left(l/\rho^2\right)_{ave}$ to yield

$$\dot{\theta}_{ave} = \left(l/\rho^2\right)_{ave} + \omega_L/\omega = 0. \tag{42}$$

Range of l	Critical ω_L/ω	Range of integer N
$\left(l/\rho^2\right)_{ave} \geq 0$	$\frac{\omega_L}{\omega} = \frac{2\pi}{NT_\rho} - \left(\frac{l}{\rho^2}\right)_{ave}$	$\frac{2\pi/T_\rho}{1+(l/\rho^2)_{ave}} < N \leq \frac{2\pi/T_\rho}{(l/\rho^2)_{ave}}$
$-1 < \left(l/\rho^2\right)_{ave} < 0$	$\frac{\omega_L}{\omega} = \frac{2\pi}{NT_\rho} - \left(\frac{l}{\rho^2}\right)_{ave}$	$N > \frac{2\pi/T_\rho}{1+(l/\rho^2)_{ave}}$
	$\frac{\omega_L}{\omega} = -\left(\frac{l}{\rho^2}\right)_{ave}$	$N \to \infty$
	$\frac{\omega_L}{\omega} = \frac{-2\pi}{NT_\rho} - \left(\frac{l}{\rho^2}\right)_{ave}$	$N \geq \frac{2\pi/T_\rho}{-(l/\rho^2)_{ave}}$
$\left(l/\rho^2\right)_{ave} \leq -1$	$\frac{\omega_L}{\omega} = \frac{-2\pi}{NT_\rho} - \left(\frac{l}{\rho^2}\right)_{ave}$	$\frac{-2\pi/T_\rho}{(l/\rho^2)_{ave}} \leq N < \frac{-2\pi/T_\rho}{1+(l/\rho^2)_{ave}}$

Table 1. The relation between critical Larmor frequency and angular quantum number l.

The critical B_c satisfying $\dot{\theta}_{ave} = 0$ produces isolated standing waves that form closed trajectories as shown in **Figure 2d**. This critical B_c nullifies the electron's net angular displacement and is called stagnation magnetic field. Because a passage through the quantum dot requires a net angular displacement equal to π, an electron with $\dot{\theta}_{ave} = 0$ is unable to pass the quantum dot and makes no contribution to the conductivity.

In a case study of $l < 0$, we consider the state of $(n, l) = (1, -1)$, whose quantum equations of motion read

$$\frac{d\rho}{d\tau} = i\frac{2\rho^4 - 11\rho^2 + 6}{2\rho(\rho^2 - 2)}, \quad \frac{d\theta}{d\tau} = \frac{-1}{\rho^2} + \frac{\omega_L}{\omega}. \tag{43}$$

The radial trajectories $\rho(\tau)$ are the same as those depicted in **Figure 3a**. Along different sets of radial trajectory, different modes of standing-wave motion are excited. According to the value of $\left(l/\rho^2\right)_{ave} = -\left(1/\rho^2\right)_{ave}$ given by Eq. (39), it is found that the trajectory set Ω_1 belongs to category (3), while the sets Ω_2, Ω_3 and Ω_4 belong to category (2), as tabulated in **Table 2**.

Typical standing waves in Ω_1, Ω_2 and Ω_3 are shown in **Figure 4** for $N = 5, 7$ and 9. We can see that the geometrical meaning of the integer N defined in Eq. (21) is just the number of electronic waves distributed on the circumference of the quantum dot. Due to $\dot{\theta}_{ave} < 0$ in Ω_1 trajectory set, as indicated in **Table 2**, the mean rotation direction of the electron in Ω_1 is clockwise. Because $\dot{\theta}_{ave}$ merely denotes the mean angular velocity, locally we may have $\dot{\theta} > 0$ during some short periods in which the electron rotates in an opposite direction as shown in **Figure 3b**.

In the state ψ, we have two stagnation frequencies at $\omega_L/\omega = \left(11 - \sqrt{73}\right)/12$ and $\omega_L/\omega = 2/3$. In the presence of magnetic stagnation, Larmor angular velocity ω_L/ω is counterbalanced by

Set	Frequency range	Critical frequency	Integer N
Ω_1	$0 \le \frac{\omega_L}{\omega} < 1$	$\frac{\omega_L}{\omega} = -\frac{73+3\sqrt{73}}{16N} + \frac{11+\sqrt{73}}{12}$	$4 \le N \le 9$
Ω_2	$\frac{11-\sqrt{73}}{12} \le \frac{\omega_L}{\omega} < 1$	$\frac{\omega_L}{\omega} = \frac{73-3\sqrt{73}}{16N} + \frac{11-\sqrt{73}}{12}$	$N \ge 4$
	$\frac{\omega_L}{\omega} = \frac{11-\sqrt{73}}{12}$	$\frac{\omega_L}{\omega} = \frac{11-\sqrt{73}}{12}$	$N \to \infty$
	$0 \le \frac{\omega_L}{\omega} < \frac{11-\sqrt{73}}{12}$	$\frac{\omega_L}{\omega} = -\frac{73-3\sqrt{73}}{16N} + \frac{11-\sqrt{73}}{12}$	$N \ge 15$
Ω_3	$\frac{\omega_L}{\omega} > \frac{2}{3}$	$\frac{\omega_L}{\omega} = \frac{2}{N} + \frac{2}{3}$	$N \ge 7$
	$\frac{\omega_L}{\omega} = \frac{2}{3}$	$\frac{\omega_L}{\omega} = \frac{2}{3}$	$N \to \infty$
	$0 \le \frac{\omega_L}{\omega} < \frac{2}{3}$	$\frac{\omega_L}{\omega} = -\frac{2}{N} + \frac{2}{3}$	$N \ge 3$
Ω_4	$\frac{\omega_L}{\omega} > \frac{2}{3}$	$\frac{\omega_L}{\omega} = \frac{1}{N} + \frac{2}{3}$	$N \ge 4$
	$\frac{\omega_L}{\omega} = \frac{2}{3}$	$\frac{\omega_L}{\omega} = \frac{2}{3}$	$N \to \infty$
	$0 \le \frac{\omega_L}{\omega} < \frac{2}{3}$	$\frac{\omega_L}{\omega} = -\frac{1}{N} + \frac{2}{3}$	$N \ge 2$

Table 2. Distribution of the critical frequencies in the state $(n, l) = (1, -1)$.

the quantum angular velocity $\left(l/\rho^2\right)_{ave}$ such that the electron's net angular displacement $\Delta\theta_{ave}$ is zero and the electron is stagnated within the quantum dot. The instantaneous dynamics of $\rho(\tau)$ and $\theta(\tau)$ are solved from Eq. (43) at the stagnation frequency $\omega_L/\omega = 2/3$ and the results are shown in **Figure 3c**. As expected, the net change of $\theta(\tau)$ is zero after a period of oscillation. The projection of the computed complex trajectory on the real $x-y$ plane is a closed path as illustrated in **Figure 2d**. This closed path produced by magnetic stagnation isolates the electron from the exit of the quantum dot and is the main cause of electronic resistance.

Apart from the consequence of $\dot{\theta}_{ave} = 0$, the effect of magnetic stagnation is also reflected in the wave number N. From Eq. (21), the relation between $\dot{\theta}_{ave}$ and N can be expressed by

$$N = \frac{2\pi/T_\rho}{\theta_{ave}} = \frac{2\pi/T_\rho}{\left(l/\rho^2\right)_{ave} + \omega_L/\omega} \tag{44}$$

There are infinitely many wavelengths distributed on the circumference of the quantum dot, as $\dot{\theta}_{ave}$ approaches to zero. The variation of the wave number N with respect to the critical Larmor frequency ω_L/ω for the quantum state $(n,l) = (1,-1)$ is demonstrated in **Figure 5a**. A prominent change of N appears in the vicinity of the two stagnation frequencies $\omega_L/\omega = \left(11-\sqrt{73}\right)/12$ and $2/3$, at which the wave number N approaches to infinity. These two stagnation frequencies

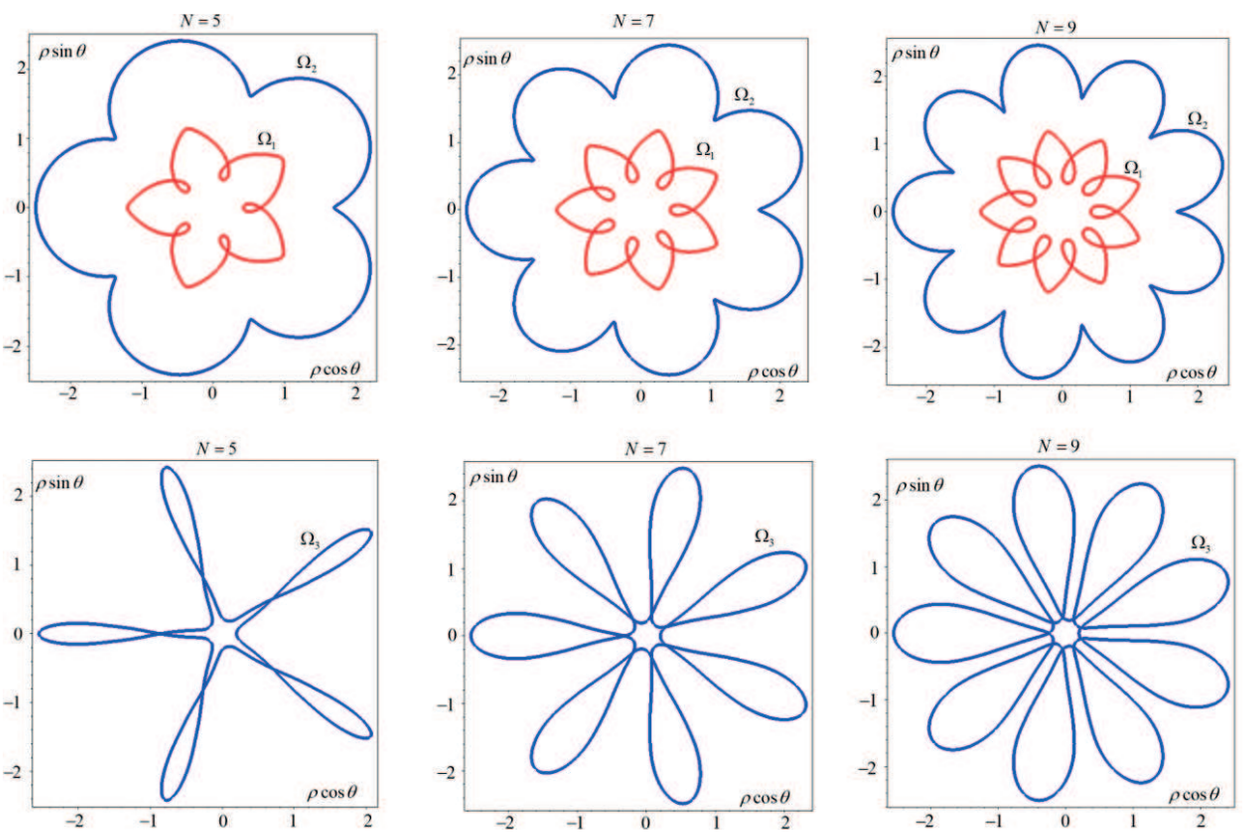

Figure 4. Typical standing-wave motions in the state $(n,l) = (1,-1)$ with wave number $N = 5$,7 and 9. The trajectory sets Ω_1, Ω_2, and Ω_3 refer to the three sets of radial trajectory defined in **Figure 3a**.

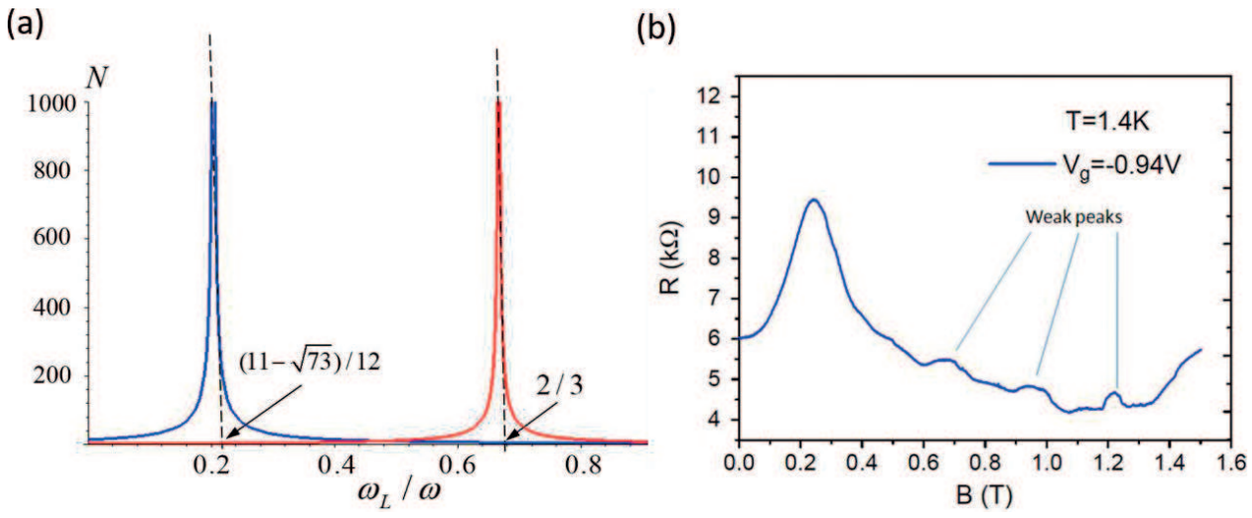

Figure 5. (a) The variation of wave number N with respect to the Larmor frequency ω_L/ω in the quantum state $(n,l)=(1,-1)$. (b) The two stagnation frequencies, $\omega_L/\omega=\left(11-\sqrt{73}\right)/12$ and 2/3, coincide with the two peaks of the experimental curve of resistance.

coincide with the locations of the resistance peaks by comparing with the experimental results as shown in **Figure 5b**.

4. Experimental verification

This section will compare the above theoretical predictions with the existing experimental data [4, 13] to confirm the fact that the effect of magnetic stagnation is the main cause to the resistance oscillation of quantum dots in low magnetic field. The experiment was performed in an AlGaAs/GaAs heterostructure with a carrier concentration $n_e=2.5\times10^{11}\text{cm}^{-2}$. Resistance was measured at temperature $T=1.4K$ using a sensitive lock-in amplifier at currents of typically 1 nA and a frequency of 12 Hz. The resulting resistance measurement in the range of low magnetic field $B\leq1.3$ is depicted in **Figure 5b** showing a strong peak located around $B=0.22\text{T}$ and three weak peaks at $B=0.65\text{T}$, 0.97T, and 1.21T.

Thus far, our analysis on quantum trajectory focuses on some specific states. In order to know the influence of the applied magnetic field on the resistance, we have to consider all the possible quantum states occupied in the device. At temperature $T=1.4K$, where the resistance is measured, the possible states to be occupied can be estimated by the Fermi-Dirac distribution,

$$f(E)=\frac{1}{1+e^{\left(E_{n,l}-E_F\right)/k_BT}}, \tag{45}$$

where $E_{n,l}$ is the energy level given by Eq. (17), and $E_F=8.5$ meV is the Fermi energy of the AlGaAs/GaAs heterostructure. All the possibly occupied states and their associated stagnation frequencies are listed in **Table 3**.

ω_L/ω		n				
		0	**1**	**2**	**3**	**4**
l	0	0	0	0	0	0
	−1	2/3	2/3, 0.205	2/3, 0.373, 0.119	2/3, 0.52, 0.19	2/3, 0.252, 0.124
	−2	4/5	4/5, 0.316	4/5, 0.543, 0.2	4/5, 0.73, 0.31, 0.146	0.4, 0.213, 0.115
	−3	6/7	6/7, 0.391	6/7, 0.64, 0.26	0.39, 0.196	*
	−4	8/9	8/9, 0.445	0.7, 0.3, 8/9	0.454, 0.237	*
	−5	*	0.486	0.75, 0.347	*	*
	−6	*	0.52	0.78, 0.38	*	*
	−7	*	0.546	*	*	*
	−8	*	0.57	*	*	*

Table 3. Stagnation frequencies ω_L/ω evaluated in the quantum states (n,l) at T = 1.4 K.

An incident electron subjected to an applied magnetic field B may enter any one of the occupied states listed in **Table 3**. The electronic resistance induced by B depends on the global transportation behavior across the quantum dot through all the allowable states. Magnetic stagnation slows down the electron's angular rate and retards the passage of the electron. The angular motion is fully retarded and the electron is trapped in the quantum dot without contribution to the conductance, as $\dot{\theta}_{ave} \to 0$. To quantify the effect of magnetic stagnation, we define a magneto-stagnation function as following

$$S(B) = -\sum_{n,\,l} \ln\left|\dot{\theta}_{ave}(n,l,B)\right| = -\sum_{n,\,l} \ln\left|\frac{\omega_L}{\omega} + \left(\frac{l}{\rho^2}\right)_{ave}\right|_{n,\,l} \tag{46}$$

where the summation is taken over all the states listed in **Table 3**. The expression of ω_L/ω as a function of B has already been given by Eq. (22). Upon comparing the prediction of Eq. (46) with the experimental results, we evaluate the constants in ω_L/ω according to the experimental setup [4, 13], which gave $\hbar\omega_c = \hbar eB/m = 1.76B\ \ meV$and $\hbar\omega_0 = \hbar\sqrt{k/m} = 0.64meV$. Using these data in Eq. (22) yields

$$\frac{\omega_L}{\omega} = \frac{0.88B}{\sqrt{0.4096 + 0.7744B^2}} \tag{47}$$

which in turn is substituted into Eq. (46) to express the magneto-stagnation function $S(B)$ as an explicit function of B.

The electron's total angular velocity via all admissible quantum states at $T = 1.4K$ can be estimated by the function $S(B)$. Because of $S(B) \to \infty$ as $\dot{\theta}_{ave} \to 0$, a large value of $S(B)$ implies that there is a high resistance to the electron's angular movability. Accordingly, $S(B)$ can be reasonably treated as an alternative description of electronic resistance. **Figure 5a** and **b** illustrates the first

evidence of this correspondence. At the two stagnation frequencies $\omega_L/\omega = \left(11 - \sqrt{73}\right)/12$ and $2/3$, corresponding to the two peaks of the resistance curve around $B = 0.22\text{T}$ and $B = 0.65\text{T}$, $S(B)$ approaches to infinity, even though only the state $(n, l) = (1, -1)$ is considered in **Figure 5a**.

If magnetic stagnation takes place simultaneously in many states, its effect will be amplified. Stagnation frequencies such as $\omega_L/\omega = 2/3$, $4/5$, and $6/7$ appear concurrently in different quantum states, as can be seen from **Table 3**. Because the stagnation function considers the superposition of $\ln\left|\dot{\theta}_{ave}(n, l, B)\right|$ coming from all the allowable states, the value of $S(B)$ is intensified at such stagnation frequency concurring in different states. According to the conversion formula Eq. (47), the magnetic field relating to the stagnation frequencies $\omega_L/\omega = 2/3$, $4/5$, and $6/7$ is found to be $B = 0.65\text{T}$, 0.97T, and 1.21T, respectively, which are just the locations of the three weak peaks of the resistance curve as shown in **Figure 5b**.

Figure 6 demonstrates the strong correspondence between the stagnation function $S(B)$ and the resistance curve, where the resistance curve is superposed on the gray-level plot of the stagnation function $S(B)$ with the intensity of darkness representing the magnitude of $S(B)$. As can be seen, the gray-level distribution matches closely with the resistance curve and in that the dark bands of $S(B)$ correctly locate the peaks of the resistance. The gray-level plot of $S(B)$ has several narrow dark bands and one broad dark band. The narrow dark bands come from the isolated stagnation frequencies at $\omega_L/\omega = 2/3$, $4/5$, and $6/7$, and their locations coincide with the three weak peaks of the resistance curve. The broad dark band of $S(B)$ covers the neighborhood of the strong peak of the resistance curve, which is formed by a series of closely distributed stagnation frequencies centered at $\omega_L/\omega = 0.29$, or equivalently,

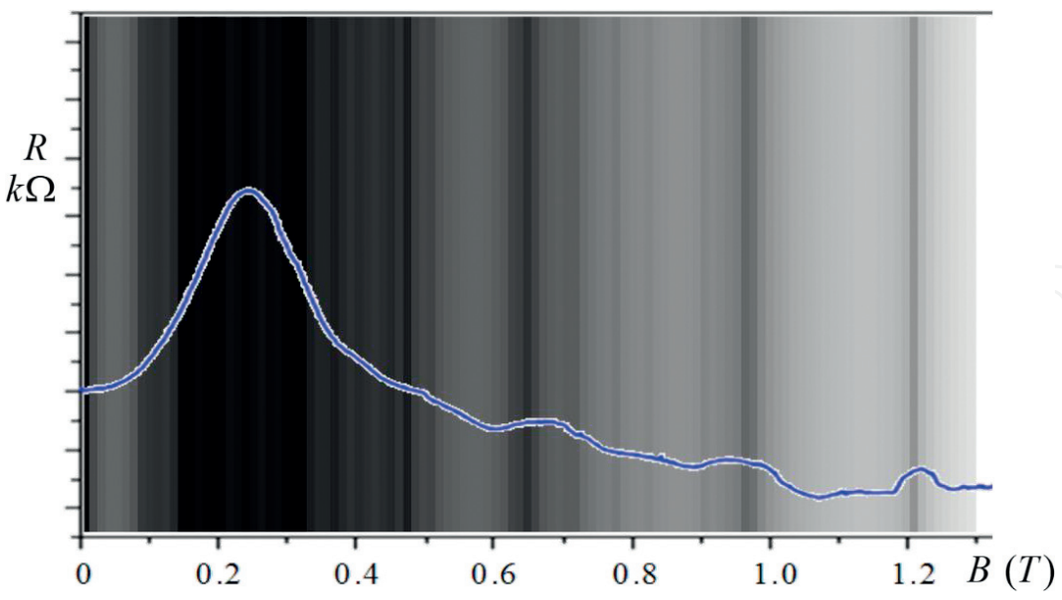

Figure 6. A gray-level plot of the stagnation function $S(B)$ with the darkness intensity representing the value of $S(B)$ is compared with the resistance curve. The resistance curve [4, 13] has a strong peak located around $B = 0.22\,\text{T}$ and three weak peaks at $B = 0.65\,\text{T}$, $0.97\,\text{T}$, and $1.21\,\text{T}$. It appears that the locations of the three narrow dark bands coincide with the three weak peaks of the resistance curve, while the broad dark band covers the neighborhood of the strong peak of the resistance curve.

http://dx.doi.org/10.5772/intechopen.74409

at $B = 0.22\,\mathrm{T}$ from Eq. (47). The agreement between the experimental data of magneto-resistance and the magneto-stagnation function $S(B)$ constructed from the quantum Hamilton dynamics Eqs. (19) and (20) is not surprising, if we recall that Eqs. (19) and (20) is fully determined by the wavefunction $\psi_{n,l}(r,\theta)$, which is responsible for the observed magneto-resistance in quantum dots.

5. Conclusions

Parallel to the existing probabilistic description for a quantum dot by a probability density function $\psi^*\psi$, this chapter considered an alternative trajectory description according to a dynamic representation of ψ constructed from quantum Hamilton mechanics. The equivalence between a given wavefunction $\psi(x)$ and its dynamic representation $\dot{x} = f(x)$ ensures that the various quantum properties possessed by ψ also manifest in its dynamic representation. The established Hamilton dynamics for a quantum dot predicts that there are special magnetic fields, which can trap electrons within the quantum dot and cause a significant raise in the resistance. The comparison with experimental data validates this theoretical prediction. Apart from the magneto-transport considered in this chapter, many other features of a quantum dot, which were studied previously from a probabilistic perspective based on ψ, now can be reexamined from a trajectory viewpoint based on the dynamic representation of ψ proposed here.

Author details

Ciann-Dong Yang* and Shih-Ming Huang

*Address all correspondence to: cdyang@mail.ncku.edu.tw

Department of Aeronautics and Astronautics, National Cheng Kung University, Tainan, Taiwan

References

[1] Ochiai Y, Widjaja AW, Sasaki N, Yamamoto K, Akis R, Ferry DK, Bird JP, Ishibashi K, Aoyagi Y, Sugano T. Backscattering of ballistic electrons in a corrugated-gate quantum wire. Physical Review B. 1997;**56**:1073-1076

[2] Lin LH, Aoki N, Nakao K, Ishibashi K, Aoyagi Y, Sugano T, Holmberg N, Vasileska D, Akis R, Bird JP, Ferry DK, Ochiai Y. Magneto-transport in corrugated quantum wires. Physica E: Low-dimensional Systems and Nanostructures. 2000;**7**:750-755

[3] Aoki N, Brunner R, Burke AM, Akis R, Meisels R, Ferry DK, Ochiai Y. Direct imaging of electron states in open quantum dots. Physical Review Letters. 2012;**108**:136804

[4] Brunner R, Meisels R, Kuchar F, ElHassan M, Bird JP, Ishibashi K. Investigations of backscattering peaks and of the nature of the confining potential in open quantum dots. Physica E: Low-dimensional Systems and Nanostructures. 2004;**21**:491-495

[5] Brunner R, Meisels R, Kuchar F, Akis R, Ferry DK, Bird JP. Classical and quantum dynamics in an array of electron billiards. Physica E: Low-dimensional Systems and Nanostructures. 2008;**40**:1315-1318

[6] Brunner R, Meisels R, Kuchar F, Akis A, Ferry DK, Bird JP. Magneto-transport in open quantum dot arrays at the transition from low to high magnetic field: Regularity and chaos. International Journal of Modern Physics B. 2007;**21**:1288-1296

[7] Morfonios CV, Schmelcher P. Control of Magnetotransport in Qunatum Billiards. Switzerland: Springer International Publishing; 2017

[8] Fransson J, Kang M, Yoon Y, Xiao S, Ochiai Y, Reno J, Aoki N, Bird JP. Tuning the Fano resonance with an intruder continuum. Nano Letters. 2014;**14**:788-793

[9] Poniedziałek MR, Szafran B. Multisubband transport and magnetic deflection of Fermi electron trajectories in three terminal junctions and rings. Journal of Physics. Condensed Matter. 2012;**24**:085801

[10] Yang CD. Quantum Hamilton mechanics Hamilton equations of quantum motion, origin of quantum operators, and proof of quantization axiom. Annals of Physics. 2006;**321**: 2876-2926

[11] Yang CD. Complex mechanics. In: Progress in Nonlinear Science. Vol. 1. Hong Kong: Asian Academic Publisher; 2010

[12] Yang CD. Modeling quantum harmonic oscillator in complex domain. Chaos, Solitons, & Fractals. 2006;**30**:342-362

[13] Elhassan M, Akis R, Bird JP, Ferry DK, Ida T, Ishibashi K. Magnetically induced Bragg scattering of electrons in quantum-dot crystals. Physical Review B. 2004;**70**:205341

[14] Ferry DK, Burke AM, Akis R, Brunner R, Day TE, Meisels R, Kuchar F, Bird JP, Bennett BR. Open quantum dots-probing the quantum to classical transition. Semiconductor Science and Technology. 2011;**26**:043001

[15] Yang CD. Wave-particle duality in complex space. Ann. Physics. 2005;**319**:444-470

[16] Yang CD. Complex tunneling dynamics. Chaos,Solitons and Fractals. 2007;**32**:312-345

[17] Yang CD. Trajectory interpretation of the uncertainty principle in 1D systems using complex Bohmian mechanics. Physics Letters A. 2008;**372**:6240-6253

[18] Bohm D. A suggested interpretation of the quantum theory in terms of hidden variables. Physical Review. 1952;**85**:166-193

[19] Holland PR. The Quantum Theory of Motion. Cambridge: Cambridge University Press; 1993

[20] Chou CC, Sanz AS, Miret-Artes S, Wyatt RE. Hydrodynamic view of wave-packet interference: Quantum caves. Physical Review Letters. 2009;**102**:250401

[21] Wyatt RE, Rowland BA. Computational investigation of wave packet scattering in the complex plane: Propagation on a grid. Journal of Chemical Theory and Computation. 2009;**5**:443-451

[22] Darwin CG. The diamagnetism of the free electron. Mathematical Proceedings of the Cambridge Philosophical Society. 1931;**27**:86-90

IntechOpen